Quantum Electronics **49** (6) 563–569 (2019)

https://doi.org/10.1070/QEL17045

Active region of a functionally integrated laser–modulator

E.A. Ryndin, B.G. Konoplev

Abstract. **A method for the functional integration of injection lasers and modulators of generated light in a single heterostructure with spatially displaced quantum wells in the conduction and valence bands, formed by the second-type heterojunctions, is proposed. The structures and energy band diagrams of the active regions of functionally integrated lasers–modulators with amplitude and frequency modulation are considered. A physical–topological model and a technique for numerical simulation of lasers–modulators is proposed. It is shown that the maximum modulation frequencies for the proposed heterostructures, in contrast to the same frequencies implemented under pump current modulation, are not limited by the duration of transients in the laser power supply circuit and the carrier lifetime in the laser active region but are determined by the photon lifetime in the cavity.**

Keywords: *functionally integrated injection laser–modulator, amplitude and frequency modulation, heterostructure.*

1. Introduction

The problem of key importance in the developments aimed at increasing the degree of integration of modern ultralarge-scale integrated (ULSI) circuits and, in particular, increasing the number of cores on crystals is the insufficient efficiency of the currently used core–core connections. The modern metal core–core connections cease to satisfy the growing requirements to the operating speed, energy efficiency, and noise immunity [1].

One of the ways to solve this problem is to replace metal lines (elements of critical importance) with integrated optical connections, which transfer amplitude-modulated laser radiation with much higher energy efficiency and operating speed.

The functional possibilities of integrated optical switching systems can be extended using not only amplitude but also frequency modulation of laser radiation. For example, organic materials with bistable photochromic molecules, which change their properties under illumination at a certain wavelength, are widely applied as a base for molecular electronics elements. Synthesis of new photochromic organic materials opens ways to design integrated molecular electronics devices with unique characteristics: ultrahigh packing density and operating speed, which cannot be implemented by means of modern silicon electronics [2–4]. However, these devices cannot be designed without matching the main characteristics of bistable organic molecules with the parameters of frequency-modulated laser pulses, which control the state of these molecules or molecular ensembles. This primarily concerns the maximum value of laser beam modulation frequency.

At the same time, we should note the following. As applied to modern multicore ULSI circuits, the efficiency of integrated optical connections is significantly reduced due to the conversion of electrical signals into optical at the input and, correspondingly, optical signals into electrical at the output. As a result, a need arises in the development and implementation of integrated optical switching systems, whose generalised block diagram is presented in Fig. 1. The main elements of this commutation system, along with optical communication line, are integrated injection laser, light modulator, and photodetector. Currently, the characteristics of optical modulators and photodetectors limit to a great extent the efficiency of the integrated optical connections under consideration [1].

The amplitude modulation of laser radiation in optical switching systems is performed using different methods. In particular, widespread modulation techniques are based on the use of laser pump current and external modulators (acousto-optic, electro-optic, etc.) [5, 6].

When modulating by the pump current, the maximum modulation frequency is limited by the duration of transients in the laser power supply circuit, which is determined by the pump current and the carrier lifetime in the active region.

When using external modulators, the maximum modulation frequency is limited by the duration of transients in modulators (on the order of 0.1–1 ns). However, additional problems of technological compatibility between the semiconductor lasers and materials used in external modulators may arise in this case [7–14].

Our purpose was to develop a method of functional integration of an injection laser and an optical modulator in a single heterostructure in order to increase the maximum laser modulation frequency, extend the functional possibilities of this system (implementation of both amplitude and frequency modulation techniques), and provide its technological compatibility.

2. Structures of functionally integrated lasers–modulators

The structures of the active regions of functionally integrated injection lasers–modulators with amplitude and frequency modulation of generated light are schematically shown in Figs 2 and 3, respectively [15, 16].

E.A. Ryndin, B.G. Konoplev Southern Federal University, Bol'shaya Sadovaya ul. 105/42, 344006 Rostov-on-Don, Russia;
e-mail: earyndin@sfedu.ru, kbg@sfedu.ru

Received 18 April 2019
Kvantovaya Elektronika **49** (6) 563–569 (2019)
Translated by Yu.P. Sin'kov

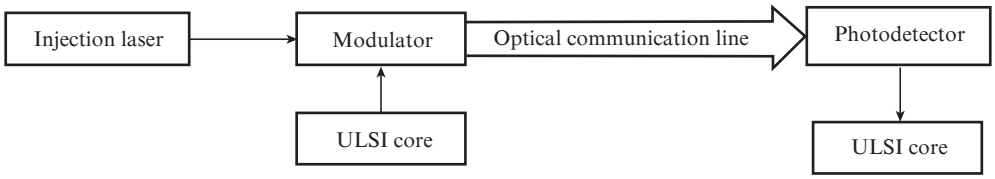

Figure 1. Generalised block diagram of the system for optical switching of ULSI cores.

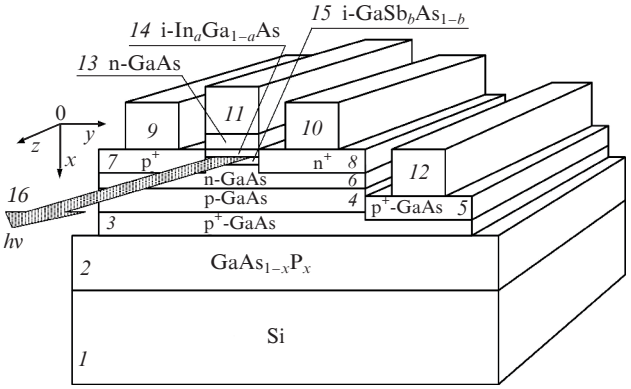

Figure 2. Structure of the active region of a laser–modulator with amplitude modulation: (*1*) silicon substrate; (*2*) gradient buffer layer $GaAs_{1-x}P_x$; (*3*) heavily doped p^+-GaAs layer of the control p–n junction; (*4*) p-GaAs layer of the control p–n junction; (*5*) p^+ region of control contact *12*; (*6*) n-GaAs layer of the control p–n junction; (*7*, *8*) p^+ and n^+ power supply regions; (*9*, *10*) power supply contacts; (*11*, *12*) control contacts; (*13*) n-GaAs region of the control Schottky junction; (*14*, *15*) laser–modulator active region: second-type heterojunction i-$In_aGa_{1-a}As$/i-$GaSb_bAs_{1-b}$; (*16*) laser beam [15].

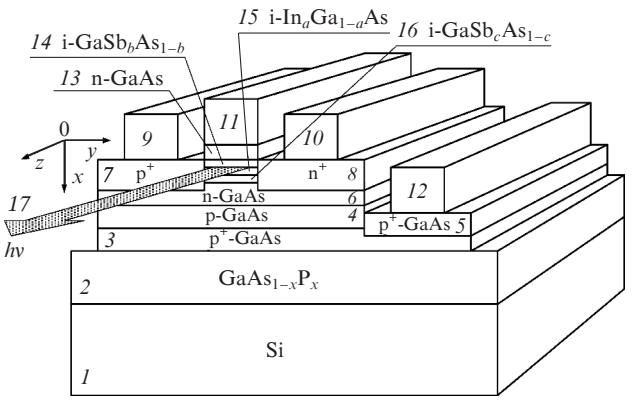

Figure 3. Structure of the active region of a laser–modulator with frequency modulation: (*1*) silicon substrate; (*2*) gradient buffer layer $GaAs_{1-x}P_x$; (*3*) heavily doped p^+-GaAs layer of the control p–n junction; (*4*) p-GaAs layer of the control p–n junction; (*5*) p+ region of control contact *12*; (*6*) n-GaAs layer of the control p–n junction; (*7*, *8*) p^+ and n^+ power supply regions; (*9*, *10*) power supply contacts; (*11*, *12*) control contacts; (*13*) n-GaAs region of the control Schottky junction; (*14*–*16*) laser–modulator active region: i-$GaSb_bAs_{1-b}$/i-$In_aGa_{1-a}As$/i-$GaSb_cAs_{1-c}$ heterostructure; (*17*) laser beam [16].

Each structure contains a p–n junction (regions *7* and *8* with power supply contacts for lasers *9* and *10*), oriented so that the pump current flows along the *y* axis. The active region of this p–n junction contains a heterostructure of either amplitude (regions *14* and *15* in Fig. 2) or frequency (regions *14*–*16* in Fig. 3) modulator with control contacts *11* and *12* and two control junctions: a Schottky junction (between n-GaAs region *13* and contact *11*) and a p–n junction (regions *3*–*6*).

Buffer gradient layer *2* ($GaAs_{1-x}P_x$), in correspondence with the data of [17], makes it possible to grow a single-crystal GaAs layer on a silicon substrate.

3. Principle of laser operation

The principle of operation of a laser–modulator with amplitude modulation of generated light is illustrated by the energy band diagrams of the integrated modulator and the spatial distributions of electron and hole concentrations, which are schematically shown in Fig. 4.

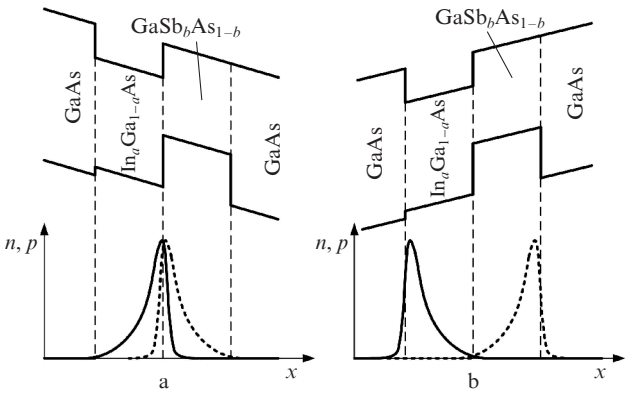

Figure 4. Energy band diagrams (top) of an integrated amplitude modulator and spatial distributions of the electron concentration $n(x)$ (solid lines) and hole concentration $p(x)$ (dashed lines) at (a) negative and (b) positive directions of the control field and a constant pump current.

The element operates as follows. A steady-state pump current is fed to the laser power supply circuit (contacts *9* and *10* in Fig. 2). This current (flowing along the *y* axis) exceeds the threshold value; i.e., when the direction of the transverse (oriented along the *x* axis) control field corresponds to that shown in Fig.4a, the pump current provides fulfilment of lasing conditions and formation of a laser beam in the direction of the *z* axis. The laser radiation is modulated at a constant pump current by changing (to opposite) the direction of the transverse field formed by control contacts *11* and *12* (Fig. 2), which leads to spatial rearrangement (along the *x* axis) of the carrier concentration peaks in spatially displaced quantum wells (QWs) 14 and 15 of the heterostructure in Fig. 2, which are formed by the second-type heterojunction i-$In_aGa_{1-a}As$/i-$GaSb_bAs_{1-b}$.

At the control field direction corresponding to that in Fig. 4a, the peaks of electron and hole concentrations are aligned at the interface, due to which the lasing intensity

increases. A change in the control field direction, in correspondence with Fig. 4b, causes spatial separation of electron and hole concentration peaks in the modulator QWs, as a result of which the laser beam intensity decreases, and thus amplitude modulation is implemented.

The principle of operation of a laser–modulator with frequency modulation is illustrated by the energy band diagram and spatial distributions of electron and hole concentrations, which are schematically presented in Fig. 5 [18, 19].

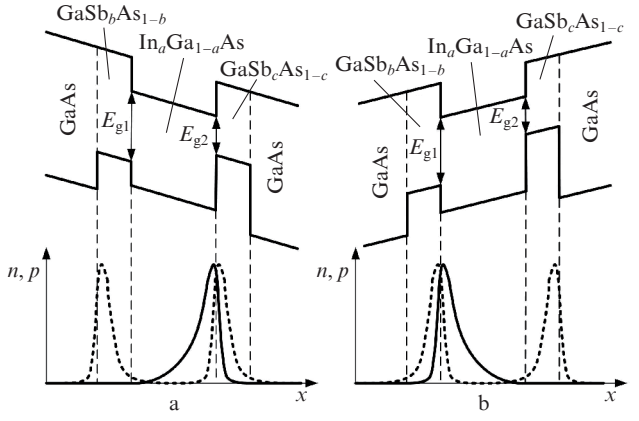

Figure 5. Energy band diagrams (top) of an integrated frequency modulator and spatial distributions of the electron concentration $n(x)$ (solid lines) and hole concentration $p(x)$ (dashed lines) at (a) negative and (b) positive directions of the control field and a constant pump current [18, 19].

In this case, similar to the laser with amplitude modulation, a steady-state pump current (which flows along the y axis and exceeds the threshold value) is fed to the supply circuit (contacts *9* and *10* in Fig. 3), while the direction of the transverse control field changes along the x axis in correspondence with a change in the voltage applied across control contacts *11* and *12* (Fig. 3). A change in the control field direction leads to a spatial alignment of carrier concentration peaks in the QWs of the conduction and valence bands, separated by a band gap E_{g1} (Fig. 5a) or E_{g2} (Fig. 5b). As a result, the wavelength of generated laser radiation changes in correspondence with the change in the direction of transverse control field, taking values λ_1 or λ_2; i.e., frequency modulation is provided.

The pump current and, correspondingly, the level of electron and hole injection into the laser–modulator active region are steady. Therefore, at a fast change in the direction of the transverse control field, a spatial rearrangement of carrier concentration peaks occurs at a practically constant total number of carriers in the modulator QWs (regions *14–16* in Fig. 3). As a result, the maximum laser beam modulation frequency is determined by not the relatively inertial transients in the laser power supply circuit and the carrier lifetime in the active region but the time of transverse-field-controlled rearrangement of electron and hole concentration peaks in the QWs of the conduction and valence bands, which, according to the results of numerical simulation [20], is less than 0.2 ps, depending on the QW and potential barrier parameters; this time correspond to THz frequencies. The estimate of the spatial rearrangement time of carrier concentration peaks in QWs [20] was obtained by numerical simulation disregarding the influence of the electrical capacitance of device on the leading edge duration and the shape of the control signal.

The presence of two peaks (at the wavelengths λ_1 and λ_2) in the spectrum of frequency-modulated laser radiation increases the efficiency of conversion and transfer of two-level logic signals through optical channels. With allowance for the presence of peaks at the wavelengths λ_1 and λ_2 in the spectrum of functionally integrated laser–modulator, the laser cavity length should be simultaneously multiple of $\lambda_1/2$ and $\lambda_2/2$.

Frequency modulation can also be implemented using two injection lasers with integrated amplitude modulators, one of which generates at the wavelength λ_1 and the other generates at the wavelength λ_2. The corresponding connection scheme of lasers–modulators is shown in Fig. 6.

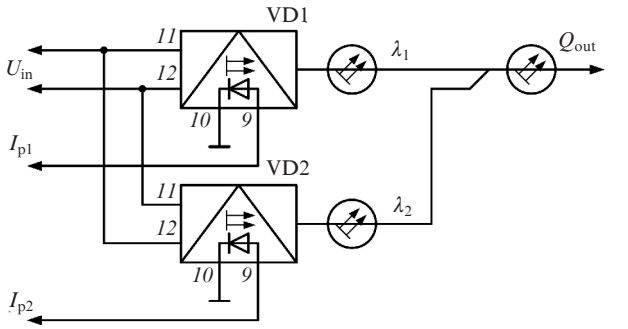

Figure 6. Schematic of the connection of lasers VD1 and VD2 with integrated amplitude modulators for implementing laser beam frequency modulation (the numbers of contacts correspond to Fig. 2):
U_{in} is the control voltage; I_{p1} and I_{p2} are the pump currents of lasers–modulators VD1 and VD2, respectively; λ_1 and λ_2 are the wavelengths of VD1 and VD2; and Q_{out} is the frequency-modulated output optical signal.

In this case, steady-state pump currents I_{p1} and I_{p2} (exceeding the threshold values) are fed into the power supply circuits of lasers VD1 and VD2 (contacts *9* and *10* in Fig. 6); a modulation voltage U_{in} is supplied in antiphase to control contacts *11* and *12* of modulators of the first and second lasers; and the laser beams with wavelengths λ_1 and λ_2, amplitude-modulated in antiphase, are transmitted through an optical connector to the output optical line to form a frequency-modulated optical signal Q_{out} in this line.

4. Model

One of the main stages in the development of any device is its simulation for theoretical justification of the suggestions about the character of physical processes occurring in this device. Kinetics equations are widely used to simulate the transients in injection lasers; these equations are modified with allowance for the specific features of laser structures under study [21–24]. However, kinetics equations cannot be used to simulate the active regions of functionally integrated lasers–modulators considered here, because they are ordinary differential equations, which do not take into account the nonuniformity and difference in the spatial distributions of electron and hole concentrations in the active region of the structure and the influence of the periphery (primarily, the control junctions) on the laser–modulator operation.

To solve this problem, we constructed a system of partial differential equations [25]

$$\nabla(\varepsilon\nabla\varphi) = \frac{e}{\varepsilon_0}(n - p - N), \tag{1}$$

$$\frac{\partial n}{\partial t} = \nabla\{\mu_{\rm n}[-n\nabla(\varphi + V_n) + \varphi_T\nabla n]\} - \frac{\sqrt{np - n_{\rm i}^2}}{\tau_{\rm s}} - v_g g(n,p,n_{\rm ph})n_{\rm ph}, \tag{2}$$

$$\frac{\partial p}{\partial t} = \nabla\{\mu_{\rm p}[p\nabla(\varphi - V_{\rm p}) + \varphi_T\nabla p]\} - \frac{\sqrt{np - n_{\rm i}^2}}{\tau_{\rm s}} - v_g g(n,p,n_{\rm ph})n_{\rm ph}, \tag{3}$$

$$\frac{\partial n_{\rm ph}}{\partial t} = -\frac{n_{\rm ph}}{\tau_{\rm ph}} + \beta\frac{\sqrt{np - n_{\rm i}^2}}{\tau_{\rm s}} + v_g g(n,p,n_{\rm ph})n_{\rm ph}, \tag{4}$$

which satisfies the aforementioned requirements. It includes the Poisson equation (1); continuity equations for electrons (2) and holes (3) in the diffusion–drift approximation, supplemented with a term describing the processes of spontaneous and stimulated radiative recombination; and the kinetics equation for photons (4), which is generalised to the case of nonuniform coordinate distributions of carriers and photons. In this system of equations,

$$g(n,p,n_{\rm ph}) = \frac{g_0}{\sqrt{1 + \varepsilon_E\Gamma n_{\rm ph}}} \times \ln\left[\frac{A(np - n_{\rm i}^2)^{1/2} + B(np - n_{\rm i}^2) + C(np - n_{\rm i}^2)^{3/2}}{An_0 + Bn_0^2 + Cn_0^3}\right]; \tag{5}$$

n and p are, respectively, the electron and hole concentrations; $n_{\rm ph}$ is the photon density; $n_{\rm i}$ is the intrinsic concentration; N is the effective impurity concentration; φ is the electrostatic potential; φ_T is the temperature potential; $V_{\rm n}$ is the heterostructural potential in the conduction band; $V_{\rm p}$ is the heterostructural potential in the valence band; $\mu_{\rm n}$ is the electron mobility; $\mu_{\rm p}$ is the hole mobility; ε is the semiconductor permittivity; ε_0 is the permittivity of free space; e is the elementary charge; $g(n,p,n_{\rm ph})$ is the optical gain; β is the fraction of spontaneous radiation in a laser mode; t is time; $\tau_{\rm s}$ is the spontaneous recombination time constant; $\tau_{\rm ph}$ is the photon lifetime in the laser–modulator cavity; $v_{\rm g}$ is the photon velocity in the laser–modulator active region; n_0 is the threshold carrier concentration; Γ is the optical confinement factor; ε_E is the factor determining the sum of the effects of optical amplification reduction; g_0 is a proportionality factor; A and B are, respectively, the trapping and radiative recombination coefficients; and C is the Auger recombination coefficient.

Dirichlet boundary conditions were imposed on the control contacts of laser–modulator for a given control voltage. The boundary conditions on the supply contacts of laser–modulator for a given pump current density had the form

$$\frac{\partial\varphi}{\partial\zeta} = \frac{j + \mu_{\rm n}\left(\frac{\partial n}{\partial\zeta} - n\frac{\partial V_{\rm n}}{\partial\zeta}\right) - \mu_{\rm p}\left(\frac{\partial p}{\partial\zeta} - p\frac{\partial V_{\rm p}}{\partial\zeta}\right)}{\mu_{\rm n}n + \mu_{\rm p}p},$$

$$n = \frac{N}{2} + \sqrt{\left(\frac{N}{2}\right)^2 + n_{\rm i}^2},\ p = -\frac{N}{2} + \sqrt{\left(\frac{N}{2}\right)^2 + n_{\rm i}^2},\ n_{\rm ph} = 0, \tag{6}$$

where j is the laser–modulator pump current density and ζ is the normal to the contact boundary. Neumann boundary conditions were imposed on the boundaries free of contacts:

$$\frac{\partial\varphi}{\partial\zeta} = 0,\quad \frac{\partial n}{\partial\zeta} = 0,\quad \frac{\partial p}{\partial\zeta} = 0,\quad \frac{\partial n_{\rm ph}}{\partial\zeta} = 0. \tag{7}$$

Expression (5) for calculating the gain $g(n,p,n_{\rm ph})$ in this system of equations is based on the model proposed in [19]. This model was refined with allowance for the nonuniformity of the spatial distributions of electron and hole concentrations in the laser–modulator active region using as an argument the expressio $\sqrt{np - n_{\rm i}^2}$ instead of the concentration of electron–hole pairs, as in the terms $\sqrt{np - n_{\rm i}^2}/\tau_{\rm s}$ describing the spontaneous radiative recombination rate in Eqns (2)–(4). This expression is more correct, because it determines the degree of deviation of electron and hole concentrations from equilibrium with allowance for their nonuniform spatial distributions.

In the initial basis of variables $\{\varphi,n,p,n_{\rm ph}\}$, the system of equations (1)–(4) with boundary conditions (6) and (7) is extremely difficult for numerical analysis. To solve this problem after normalisation with the use of the factors described in [26], the right-hand sides of Eqns (1)–(4) were transferred to a combined basis of variables $\{\varphi,n,p,\Phi_{\rm n},\Phi_{\rm p},n_{\rm ph}\}$ and presented for two spatial measurements in the following dimensionless form:

$$\frac{\partial}{\partial x}\left(\varepsilon\frac{\partial\varphi}{\partial x}\right) + \frac{\partial}{\partial y}\left(\varepsilon\frac{\partial\varphi}{\partial y}\right) = \Phi_{\rm n}\exp(\varphi + V_{\rm n}) - \Phi_{\rm p}\exp(-\varphi + V_{\rm p}) - N, \tag{8}$$

$$\frac{\partial n}{\partial t} = \frac{\partial}{\partial x}\left[\mu_{\rm n}\exp(\varphi + V_{\rm n})\frac{\partial\Phi_{\rm n}}{\partial x}\right] + \frac{\partial}{\partial y}\left[\mu_{\rm n}\exp(\varphi + V_{\rm n})\frac{\partial\Phi_{\rm n}}{\partial y}\right] - \exp\left(\frac{V_{\rm n} + V_{\rm p}}{2}\right)\sqrt{\Phi_{\rm n}\Phi_{\rm p} - 1} - v_{\rm g}gn_{\rm ph}, \tag{9}$$

$$\frac{\partial p}{\partial t} = \frac{\partial}{\partial x}\left[\mu_{\rm p}\exp(-\varphi + V_{\rm p})\frac{\partial\Phi_{\rm n}}{\partial x}\right] + \frac{\partial}{\partial y}\left[\mu_{\rm p}\exp(-\varphi + V_{\rm p})\frac{\partial\Phi_{\rm p}}{\partial y}\right] - \exp\left(\frac{V_{\rm n} + V_{\rm p}}{2}\right)\sqrt{\Phi_{\rm n}\Phi_{\rm p} - 1} - v_{\rm g}gn_{\rm ph}, \tag{10}$$

$$\frac{\partial n_{\rm ph}}{\partial t} = -\frac{n_{\rm ph}}{\tau_{\rm ph}} + \beta\exp\left(\frac{V_{\rm n} + V_{\rm p}}{2}\right)\sqrt{\Phi_{\rm n}\Phi_{\rm p} - 1} + v_{\rm g}gn_{\rm ph}, \tag{11}$$

$$\Phi_{\rm n} = n\exp(-\varphi - V_{\rm n}),\quad \Phi_{\rm p} = p\exp(\varphi - V_{\rm p}), \tag{12}$$

where x and y are coordinates and $\Phi_{\rm n}$ and $\Phi_{\rm p}$ are the exponents of Fermi quasi-levels for electrons and holes. The initial conditions were determined from numerical solution of the time-independent version of the system of equations (8)–(11).

A numerical realisation of the model described by Eqns (8)–(12) was performed within the finite-element method.

The time-independent problem was solved by the Newton method, and the time-dependent problem was solved using the explicit counterflow scheme described in [27].

The adequacy of model (8)–(12) was estimated in [25] by comparing the results of numerical simulation for a conventional laser with a double heterostructure, which were obtained using the proposed model and the kinetics equations.

5. Simulation and discussion of results

The results of numerical simulation of the active region of injection laser with a functionally integrated amplitude modulator, whose structure is shown in Fig. 2, are presented in Figs 7 and 8. The main parameters of the laser–modulator active region that were applied in the simulation are listed below.

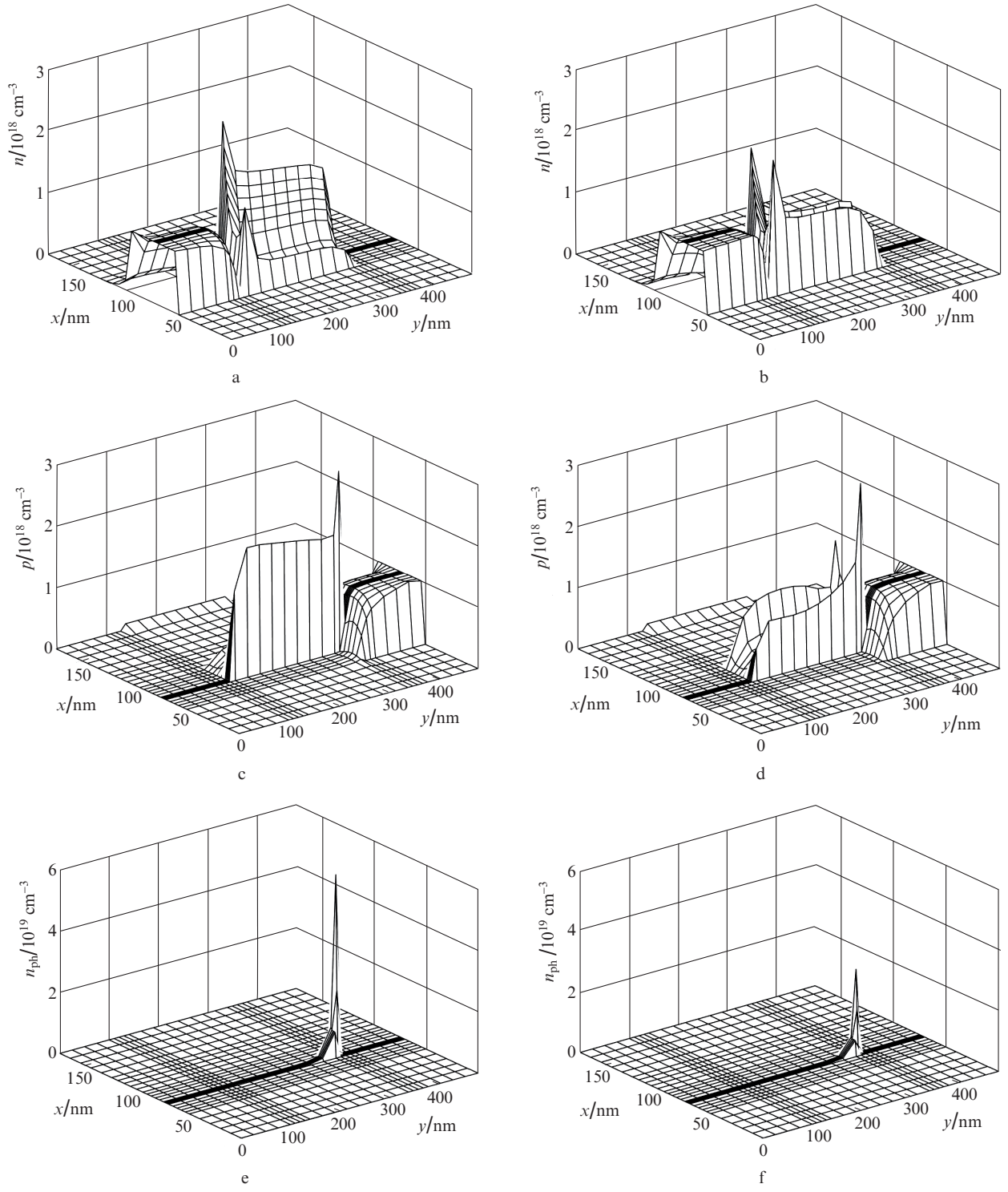

Figure 7. Spatial distributions of (a, b) electron, (c, d) hole, and (e, f) photon concentrations in the active region of laser–modulator at (a, c, e) negative and (b, d, f) positive directions of the control field.

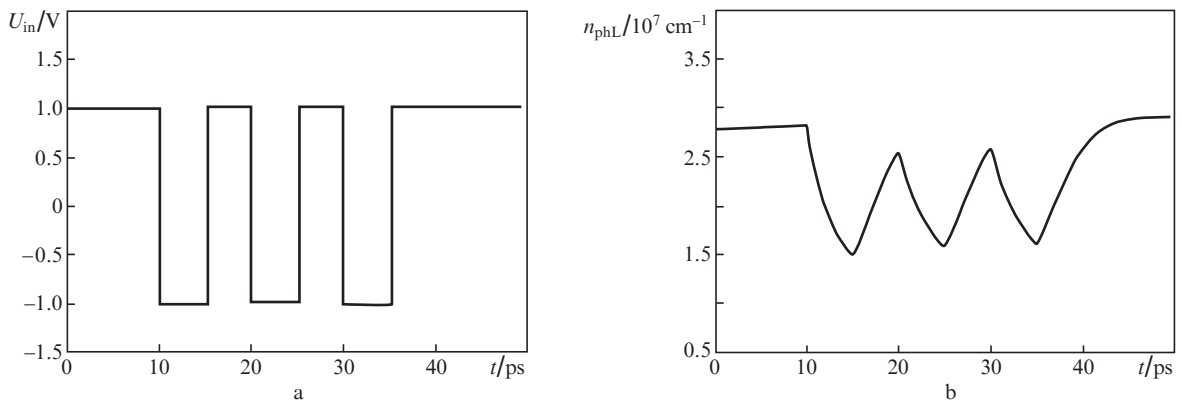

Figure 8. Time dependences of the (a) control voltage $U_{in}(t)$ and (b) linear photon density $n_{phL}(t)$ in the laser–modulator cavity.

Active-region size (distance between (regions *7* and *8* un Fig.2)/nm	200
Thickness of the i-$In_aGa_{1-a}As$/nm	.25
Thickness of the i-$GaSb_bAs_{1-b}$/nm	.25
Thickness of the n layer in the control Schottky junction/nm	.50
Donor concentration in the n layer of the control Schottky junction/cm^{-3}	10^{17}
Thickness of the n layer in the control p–n junction/nm	.30
Thickness of the p layer in the control p–n junction/nm	.45
Donor concentration in the n layer of the control p–n junction/cm^{-3}	10^{17}
Acceptor concentration in the p layer of the control p–n junction/cm^{-3}	10^{17}
Impurity concentration in the p+ and n+ power supply regions/cm^{-3}	10^{18}
Photon lifetime in the cavity, τ_{ph}/ps	3
Spontaneous radiation fraction β in the laser mode	10^{-4}

The spatial distributions of electron, hole, and photon concentrations in the lasermodulator active region for a specified pump current density of 30 kA cm^{-2} at opposite directions of the transverse control field (in correspondence with Fig. 4) are presented in Fig. 7. Figure 8 shows the time dependence of the photon linear density $n_{phL}(t)$ in the laser–modulator cavity (Fig. 8b) at a pulsed change in the control voltage $U_{in}(t)$ (Fig. 8a).

The changes in the spatial distributions of charge carrier and photon concentrations, presented in Fig. 7, correspond to a transient time of 0.12 ps. The linear photon density $n_{phL}(t)$ in the cavity was determined by integrating the photon volume density $n_{ph}(x, y, t)$ over the cross-sectional area of laser–modulator active region.

The results of numerical simulation show that, in contrast to the maximum frequency for the pump current modulation, the maximum frequency for the modulation by transverse-field-controlled rearrangement of electron and hole concentration peaks for the lasers–modulators under consideration is not limited by the carrier lifetime in the active region but is determined, as follows from Fig. 8, by the photon lifetime in the cavity, which amounts to few picoseconds. As a result, the maximum modulation frequency of generated light may reach 100–300 GHz. The time of controlled rearrangement of carrier concentration peaks in the laser–modulator QWs is 0.12 ps; therefore, it cannot be considered as a factor limiting the maximum light modulation frequency.

6. Conclusions

A method of functional integration of injection lasers and light modulators in a single heterostructure was proposed in order to increase the efficiency of integrated optical core–core connections in modern ULSI circuits. This method allows one to increase the maximum modulation frequency and implement lasers with integrated modulators (of both amplitude and frequency types) in a unified technological cycle.

The structures and energy band diagrams of active regions and the principles of operation of functionally integrated lasers–modulators with amplitude and frequency modulation, based on spatially displaced QWs in the conduction and valence bands (formed by second-type heterojunctions), were considered. A possibility of implementing frequency modulation using two lasers with integrated amplitude modulators was shown.

A physical–topological model of the lasers–modulator active regions was proposed. An analysis of the numerical simulation results showed that the maximum modulation frequencies for the lasers–modulators under study, in contrast to the lasers with pump current modulation, are not limited by the duration of transients in the laser power supply circuit and the carrier lifetime in the laser active region but are determined by the photon lifetime in the cavity and may reach 100–300 GHz.

The results were obtained disregarding the structure and main parameters of the laser waveguide. An analysis of functionally integrated lasers–modulators taking into account the characteristics of the optical elements of these devices will be performed in subsequent studies.

Acknowledgements. This work was supported by the 'Programme for the Development of the Southern Federal University until 2021' (Project VnGr-07/2017-10).

References

1. Vlasov Y., Green W.M.J., Xia F. *Nat. Photonics*, **2**, 242 (2008).
2. Kawata S., Kawata Y. *Chem. Rev.*, **100** (5), 1777 (2000).
3. Higgins S. *Chim. Oggi-Chem. Today*, **21** (1-2), 63 (2003).

4. Minkin V.I. *Izv. Ross. Akad. Nauk, Ser. Khim.*, **4**, 673 (2008).
5. Morthier G. *IEEE Photonics Technol. Lett.*, **16** (7), 1616 (2004).
6. Toomey J.P., Kane D.M., Lee M.W., Shore K.A. *Opt. Express*, **18** (16), 16955 (2010).
7. Soref R., Bennett B. *IEEE J. Quantum Electron.*, **23** (1), 123 (1987).
8. Kalluri S., Ziari M., Chen A., Chuyanov V., Steier W.H., Chen D., Jalali B., Fetterman H.R., Dalton L. *IEEE Photonics Technol. Lett.*, **8** (5), 644 (1996).
9. Miller D.A.B. *Proc. IEEE*, **97** (7), 1166 (2009).
10. Edwards E.H., Audet R.M., Fei E.T., Claussen S.A., Schaevtz R.K., Tasyurek E., Rong Y., Kamins T.I., Harris J.S., Miller D.A.B. *Opt. Express*, **20** (28), 29164 (2012).
11. Vasudev A.P., Kang J.H., Park J., Liu X., Brongersma M.L. *Opt. Express*, **21** (22), 26387 (2013).
12. Kolyada N.A., Nyushkov B.N., Pivtsov V.S., Dychkov A.S., Farnosov S.A., Denisov V.I., Bagaev S.N. *Quantum Electron.*, **46** (12), 1110 (2016) [*Kvantovaya Elektron.*, **46** (12), 1110 (2016)].
13. Mukhin A.V., Velikanov S.D., Glukhodedov V.D., Zakharov N.G., Frolov Yu.N. *Quantum Electron.*, **46** (8), 682 (2016) [*Kvantovaya Elektron.*, **46** (8), 682 (2016)].
14. Kotov V.M., Averin S.V., Kotov E.V., Voronko A.I., Tikhomirov S.A. *Quantum Electron.*, **47** (2), 135 (2017) [*Kvantovaya Elektron.*, **47** (2), 135 (2017)].
15. Konoplev B.G., Ryndin E.A., Denisenko M.A. RF Patent No. 2400000 (11 March 2009).
16. Konoplev B.G., Ryndin E.A., Denisenko M.A. RF Patent No. 2520947 (7 November 2012).
17. Bolkhovityanov Yu.B., Pchelyakov O.P. *Phys. Usp.*, **51** (5), 437 (2008) [*Usp. Fiz. Nauk*, **178** (5), 459 (2008)].
18. Konoplev B.G., Ryndin E.A., Denisenko M.A. *Russ. Microelectron.*, **42** (6), 360 (2013) [*Mikroelektron.*, **42** (6), 440 (2013)].
19. Konoplev B.G., Ryndin E.A., Denisenko M.A. *Russ. Microelectron.*, **44** (3), 190 (2015) [*Mikroelektron.*, **44** (3), 220 (2015)].
20. Konoplev B.G., Ryndin E.A., Denisenko M.A. *Proc. SPIE*, **9440**, 14 (2014).
21. Eliseev P.G., Drakin A.E. *Quantum Electron.*, **26** (4), 299 (1996) [*Kvantovaya Elektron.*, **23** (4), 307 (1996)].
22. Zhou W., Liu Shaobin, Wu Jie, Zhang Xiaoliu, Tang Wu. *Quantum Electron.*, **44** (4), 289 (2014) [*Kvantovaya Elektron.*, **44** (4), 289 (2014)].
23. Zarifkar A., Ansari L., Moravvej-Farshi M.K. *Fiber Integr. Opt.*, **28**, 249 (2009).
24. Konoplev B.G., Ryndin E.A., Denisenko M.A. *Russ. Microelectron.*, **46** (3), 216 (2017) [*Mikroelektron.*, **46** (3), 236 (2017)].
25. Konoplev B.G., Ryndin E.A., Denisenko M.A. *Tech. Phys. Lett.*, **41** (6), 587 (2015) [*Pis'ma Zh. Tekh. Fiz.*, **41** (12), 48 (2015)].
26. Bubennikov A.N., Sadovnikov A.D. *Fiziko-tekhnologicheskoe proektirovanie bipolyarnykh elementov kremnievykh BIS* (Physical and Technological Design of Silicon Bipolar LSI Elements) (Moscow: Radio i svyaz', 1991).
27. Konoplev B.G., Ryndin E.A., Pisarenko I.V. *Izv. Vyssh. Uchebn. Zaved., Ser. Elektron.*, **23** (3), 217 (2018).